An efficient NixZryO catalyst for hydrogenation of bio-derived methyl levulinate to γ-valerolactone in water under low hydrogen pressure

Mengqing Sun[a,b], Jie Xia[b], Haifeng Wang[b], Xiaohui Liu[a,b,*], Qineng Xia[a,b], Yanqin Wang[a,b]

[a] *Shanghai Key Laboratory of Functional Materials Chemistry, School of Chemistry and Molecular Engineering, East China University of Science and Technology, Shanghai, 200237, PR China*
[b] *Research Institute of Industrial Catalysis, School of Chemistry and Molecular Engineering, East China University of Science and Technology, Shanghai, 200237, PR China*

ABSTRACT

γ-Valerolactone (GVL) has been identified as a key intermediate for the sustainable production of fuels and value-added chemicals. In this work, an efficient NixZryO catalyst was prepared by co-precipitation and used in the low pressure hydrogenation to prepare GVL from bio-derived methyl levulinate (ML) in aqueous solution. Several catalysts that differed in their Ni/Zr molar ratio were prepared and characterized by BET, XRD, H_2-TPR, NH_3-TPD and XPS, and they exhibited different catalytic activities in the catalytic hydrogenation reaction of ML. The best catalytic activity was realized with Ni1Zr1O, which gave a 96.9% yield of GVL by low hydrogen pressure at 0.3 MPa in the aqueous solution at 150 °C. By comparison with NiO and Raney Ni, it was found that introducing zirconium into nickel oxide remarkably enhanced the performance of the NixZryO catalysts. According to the XRD, H_2-TPR and XPS results, when a certain amount of zirconium was introduced (e.g., Ni/Zr = 1), part of the nickel either coordinated with zirconium or formed Ni_mZr_nO quasi solid solution and was not readily reduced by H_2. Theoretical calculations showed that the formed Ni − O − Zr species was superior to pure nickel or zirconium oxides for the adsorption of ML. The synergy between metallic nickel, which activated H_2, and the Ni − O − Zr species, which activated ML, was believed to expedite the production of γ-valerolactone. Moreover, Ni1Zr1O showed good catalytic stability and retained the catalytic performance even after five reaction cycles of the ML hydrogenation.

1. Introduction

γ-Valerolactone (GVL) is one of the top value-added chemical candidates listed in the US Department of Energy/National Renewable Energy Laboratory (DOE/NREL) report. It has attracted considerable attention due to its excellent physical-chemical properties and unique fuel characteristics [1,2]. Various methods have been developed to improve the synthesis of GVL from lignocellulosic biomass [3,4], C6 and C5 sugars [5–8], or levulinic acid (LA) and levulinate esters [9–11].

The direct hydrogenation of LA or levulinate esters to give GVL can be conducted in the liquid phase [12,13], the vapor phase [14–16], or supercritical CO_2 [17] with various metal catalysts. Alternatively, the production of GVL from levulinate esters has also been achieved by transfer hydrogenation using formic acid [18] or isopropanol [19–21]. In addition, hydrogen generated *in situ* by MeOH reforming [22] has also been used to synthesize GVL.

Traditionally, catalytic hydrogenation is achieved by using H_2 as the hydrogen source and the compounds of various noble metals (e.g., Ru,

Rh, Pd, Pt and Au) as the catalyst. However, these reactions have limited application because they commonly require costly catalysts, use of volatile organic additives, high hydrogen pressure, and various other harsh reaction conditions [2]. Ideally, a practical hydrogenation reaction should be able to circumvent using noble metals as the catalyst, proceed under low pressure, and use water as the solvent.

Recently, various novel heterogeneous catalysts free of noble metals have been used to successfully prepare GVL by hydrogenation, including supported Cu [23–25], CuZn [26], Ni [27–29], Ni-MoOx [30], Ni_2P [31], NiFe [32,33], NiSn [34], Co [35] and Mo_2C catalysts [36]. For example, Cu-ZrO_2 was utilized to prepare GVL from LA at 200 °C and 3.4 MPa H_2. The reaction realized complete LA conversion and 90% selectivity to GVL, and the catalyst could be reused for three times [23]. Zhang et al. showed that Ni-$Fe_{0.5}$/AC exhibited the highest activity among a series of bimetallic or monometallic catalysts and could prepare GVL from EL after reaction for 6 h at 100 °C and 4 MPa H_2, giving 99.3% conversion rate and 99.0% yield [32]. Shimazu et al. successfully converted LA into a stoichiometric amount of GVL (> 99%) by

catalytic hydrogenation with highly dispersed Ni-Sn$_x$/AlOH (x = 3.0 and 1.4) in H$_2$O at 120 °C and 4 MPa H$_2$ [34]. However, the hydrogenation of LA or levulinate esters to prepare GVL over non-noble metal heterogeneous catalysts generally requires a hydrogen pressure higher than 3 MPa.

In this paper, a series of NixZryO catalysts were prepared by co-precipitation of Ni and Zr salts. The catalysts were found to successfully convert methyl levulinate (ML) to GVL in aqueous solution by hydrogenation at low pressure (0.3 MPa). The NixZryO catalysts were compared with NiO, ZrO$_2$, and NiO/ZrO$_2$ (prepared by a wet impregnation method) to examine the role of zirconium in the NixZryO catalysts and determine the catalytically active component of NixZryO catalysts for the adsorption and activation of ML in the hydrogenation reaction. This work provides useful information for designing cost-effective and environmentally friendly metal catalysts to produce GVL from ML by catalytic hydrogenation.

2. Experimental

2.1. Chemicals

Methyl levulinate were purchased from TCI (Shanghai) development Co. Ltd. Ni (NO$_3$)$_2$·6H$_2$O (99%) was purchased from Sinopharm Chemical Reagent Co. Ltd. ZrOCl$_2$·8H$_2$O (98%) and Raney Ni was purchased from Shanghai Macklin Biochemical Co., Ltd. Other chemicals were purchased from Titan technology Co. Ltd. All purchased chemicals were used without further purification.

2.2. Catalyst preparation

NixZryO catalysts were prepared by a co-precipitation method. In a typical synthesis, Ni (NO$_3$)$_2$·6H$_2$O and ZrOCl$_2$·8H$_2$O with the required Ni/Zr molar ratio for the target material were dissolved in water (e.g. 2.92 g Ni (NO$_3$)$_2$·6H$_2$O and 3.22 g ZrOCl$_2$·8H$_2$O in 100 ml water, the Ni/Zr mole ratio is 1:1) to form a mixed solution. Sodium carbonate aqueous solution (1 M) was added into the above mixed solution until the pH became 9. The mixture was further aged for 6 h and then filtered under vacuum followed by a washing step with distilled water. After that the precipitates were dried at 100 °C overnight and calcined at 400 °C for 4 h in static air. To study the role of zirconium in NixZryO catalysts for the catalytic ML hydrogenation to GVL, the NixZryO catalysts with different Ni/Zr molar ratios (Ni/Zr = 10, 5, 3, 2, 1, 0.5, 0.33) were prepared and separately named them as Ni10Zr1O, Ni5Zr1O, Ni3Zr1O, Ni2Zr1O, Ni1Zr1O, Ni1Zr2O, Ni1Zr3O. Meanwhile, NiO and ZrO$_2$ was prepared by the same process except without adding ZrOCl$_2$·8H$_2$O or Ni (NO$_3$)$_2$·6H$_2$O respectively.

For comparison, supported NiO/ZrO$_2$ sample was prepared by a wet impregnation method. ZrO$_2$ prepared by above precipitation method was used as the support for impregnation. Then ZrO$_2$ was treated with required amount of Ni (NO$_3$)$_3$·6H$_2$O aqueous solution. The supported NiO/ZrO$_2$ catalysts was dried at 100 °C overnight and afterwards calcined in static air at 400 °C for 4 h. The theoretical Ni/Zr molar ratio was 1, which was equal to that of Ni1Zr1O catalyst.

All catalysts were reduced at 400 °C in 5% H$_2$ (balance Ar) at a flow rate of 30 ml/min prior to the reaction unless otherwise stated.

2.3. Reaction condition and product analysis

The hydrogenation of methyl levulinate (ML) was carried out in a sealed Teflon-lined stainless autoclave (30 ml), equipped with an internal thermo-controller and a pressure gauge. In a typical experiment, 0.05 g catalyst, 0.15 g ML and 5.0 g water were well mixed in the autoclave. Before the reaction, autoclave was purged with hydrogen for five times then kept at the desired pressure. It took 30 mins to heat the reactor from room temperature to the desired temperature (such as 150 °C). In order to ensure the consistency of each experiment, when

the reactor was raised to the desired temperature, the zero time was recorded. After reaction, the autoclave was cooled to room temperature by loading cooling water then opened. The liquid products were analyzed by gas chromatography. For the recycle experiments, the used Ni1Zr1O catalyst was separated using centrifugation and then it was utilized repeatedly after washed with deionized water.

The liquid products were analyzed by gas chromatography (Agilent 7890) equipped with a HP-5 column and a flame ionization detector (FID) using the internal standard method. The conversion of ML (C_{ML}) and yield of GVL (Y_{GVL}) were calculated by using the equation, respectively:

$$C_{ML}(\%) = \left(1 - \frac{n_{ML}}{n_{ML.initial}}\right) \times 100\%$$

$$Y_{GVL}(\%) = \left(\frac{n_{GVL}}{n_{ML.initial}}\right) \times 100\%$$

$n_{ML.initial}$ is the moles of initial ML in reaction solution. n_{ML} and n_{GVL} are the moles of ML and GVL in the liquid products, respectively.

2.4. Catalyst characterization

Powder X-ray diffraction (XRD) patterns were recorded on a Rigaku D/max-2550VB/PC and Cu Kα (λ = 0.15406) X-ray source operated at 40 kV and 40 mA. Each sample was scanned from 2θ = 10° to 80°. The catalysts were ground into fine powder before the analysis.

Ni and Zr contents were measured by inductively coupled plasma-atomic emission spectroscopy (ICP-AES, Agilent 725ES ICP-AES).

Nitrogen adsorption-desorption isotherms of the catalysts were measured at −196 °C on a Micromeritics ASAP 2020 M sorption analyzer. Prior to the measurements, the samples were heated in a vacuum at 200 °C for 8 h to remove moisture and volatile impurities. The surface area was calculated by Brunauer-Emmett-Teller (BET) method on basis of the desorption data. Meanwhile, the pore size distribution (PSD) was determined via a non-linear density functional theory (NLDFT) fitting based on the desorption branch. The total pore volume was estimated at a relative pressure of 0.95.

Scanning electronic microscopy (SEM) images were obtained from JEOL JSM–63602 V and Hitachi S-3400N microscopes operated at 5 kV or 15 kV, respectively. Transmission electron microscopy (TEM) images were captured using a FEI TECNAI 20S-TWIN instrument at 200 kV.

H$_2$-TPR was carried out using an apparatus (PX200, Tianjin Golden Eagle Technology Co. Ltd) under 5% H$_2$/Ar (40 ml/min), at 10 °C/min ramp rate. Samples (0.05 g) were pre-treated at 400 °C under Ar for 1 h prior to reduction in order to clean the surface.

NH$_3$-TPD was measured by a Micromeritics Chemisorb 2720 analyzer. NH$_3$ was adsorbed onto the samples by exposure to flowing 10% NH$_3$ in Ar gas mixture (50 ml/min) for 60 min at 90 °C. Residual and physical adsorbed NH$_3$ was removed by purging the samples with flowing Ar at 150 °C for 1 h. Desorption of NH$_3$ was performed by heating the samples at a rate of 10 °C/min under flowing Ar (45 ml/min).

X-ray photoelectron spectra (XPS) were acquired on an ESCALAB 250 spectrometer (Thermo Fish Scientific, Al Kα, hν = 1486.6 eV). The binding energy was corrected by C1 s orbital, which was supposed to be at 284.8 eV.

Thermogravimetric analysis (TG/DTA) of the used catalyst was performed on PerkinElmer Pyris Diamond under air with a heating rate of 10 °C/min.

All the spin-polarized density functional theory (DFT) calculations are performed with the Vienna Ab-initio Simulation Package (VASP) [37], in which the Perdew-Burke-Ernzerhof (PBE) exchange-correlation functional was applied [38]. The valence electrons, *i.e.* H (1s), C and O (2s, 2p), Ni (3d, 4s) and Zr (4d, 5s), are expanded on a set of plane waves with a kinetic cutoff of 450 eV, while core regions are treated

with pseudopotentials, as encored in the Projector Augmented Wave (PAW) approach [39]. To improve the description of the on-site Coulomb effect of Ni compound, partial occupations of Ni d-orbitals are penalized by a Hubbard parameter, which has been empirically set to 5.3 eV [40]. Moreover, to describe the van der Waals interactions induced by long-chain hydrocarbon molecules, the Grimme's DFT-D2 methodology was utilized [41]. For the NiO(100) and NiZrO(100) surface, the bottom two layers are fixed, and the upper two layers are allowed to be fully relaxed. For the tetragonal-ZrO$_2$(101) surface, the bottom two layers are fixed, and the upper one layer is relaxed. The vacuum is 20 Å to eliminate interactions between the slabs along the c direction. To build a surface slab model of NiZrO, we first optimize the bulk which contains three Ni atoms and one Zr atom. The lattice constants are computed to be a = 4.330 Å and c/a = 1. Then, the NiZrO (100) surface is constructed as a periodic 3 × 3 slab with four metal layers. Full structural relaxations are performed with convergence criteria of 10^{-4} eV and 5×10^{-2} eV/Å for the electronic and ionic loops, respectively. Brillouin zone integration is done using a 1 × 1 × 1 Monkhorst-Pack grid owing to the large surface model used here. For adsorption processes, the adsorption energies are calculated as:

$$E_{ads} = E_{adsorbate+slab} - E_{slab} - E_{adsorbate}$$

where $E_{adsorbate+slab}$ and E_{slab} are the total energy of the surface slab with and without the adsorbate covered, and $E_{adsorbate}$ is the energy of the adsorbate molecule in the gas phase. The transition states (TSs) involved in the catalytic reaction were located using the constrained minimization technique [42].

3. Results and discussion

3.1. Catalyst physical properties

The synthetic procedure for NixZryO is presented in detail in the Experimental section. The Ni/Zr molar ratios of all NixZryO samples are displayed in Table 1. As shown in Table 1, deviations between the actual Ni/Zr molar ratios (column 5, Table 1) and corresponding theoretical values (column 4, Table 1) are found. Though which means the actual Ni/Zr molar ratio became lower when x decreased or y increased, the trend remains consistent.

The N$_2$ adsorption-desorption isotherms and pore size distributions of NiO, ZrO$_2$, NiO/ZrO$_2$ and all NixZryO samples are measured. ZrO$_2$, NiO/ZrO$_2$ and all NixZryO samples are exhibited Type IV behavior pointing to porous materials. The BET surface area, pore volume and average pore diameter of these samples were listed in Table 1. It can be seen that the BET surface area and pore volume of NiO are not detected. Then the effect of the addition of nickel on the physical properties of ZrO$_2$ rather than the effect of zirconium on NiO is considered. As shown in Table 1, the BET surface area and pore volume of ZrO$_2$ are 66.7 m^2/g and 0.12 cm^3/g, respectively. After supported NiO by the wet

impregnation method, the BET surface area and pore volume of NiO/ZrO$_2$ decrease to 42.7 m^2/g and 0.09 cm^3/g, respectively while the average pore diameter remains 4.0 nm. However, incorporating NiO by the co-precipitation method significantly changes the physico-chemical properties of ZrO$_2$. The BET surface area, pore volume and average pore diameter all greatly reduce along with increasing NiO incorporation up to Ni/Zr molar ratio of around 0.5. But this trend does not continue for a further addition of NiO ($n_{Ni}/n_{Zr}=1-5$). The data in Table 1 clearly indicate that the BET surface area values of NixZryO catalysts peak at Ni3Zr1O with the largest BET surface area of 119.8 m^2/g, pore volumes and average pore diameters achieve maximum at Ni5Zr1O with 0.46 cm^3/g and 5.6 nm, respectively. This may be due that the presence of NiO is associated with the formation of rather stable Ni − O − Zr bonds on the material surface. And this interaction has been described to reduce the mobility of Zr atoms on the surface potentially suppressing sintering during calcination and increase the BET surface area [43]. While further increase of Zr content would lead to the decrease of surface area, pore volume and average pore diameter.

The powder XRD patterns of NiO, ZrO$_2$, NiO/ZrO$_2$ (prepared by wet impregnation) and NixZryO samples with different Ni/Zr molar ratios are reported in Fig. 1. The diffraction lines at 2θ = 37.2, 43.2, 62.8, 75.4 and 79.4° due to NiO phase with face centred cubic geometry are observed. For ZrO$_2$, there are two phases: diffraction lines at 2θ = 30.1, 35.0, 50.2 and 59.7° are attributed to cubic ZrO$_2$ phase (c-ZrO$_2$) and diffraction lines at 2θ = 24.0, 28.2, 31.5, 34.2, 40.7, 45.5 and 55.4° are attributed to monoclinic ZrO$_2$ phase (m-ZrO$_2$). As shown in Fig. 1, with the addition of zirconium, the intensity of NiO diffraction lines weakened gradually to almost zero when Ni/Zr molar ratio approached 1. At the same time, a broad diffraction peak of ZrO$_2$ phase at around 30° became obvious. In contrast, there are distinct diffraction lines of NiO and ZrO$_2$ phase in the NiO/ZrO$_2$ sample prepared using a wet impregnation method. This variation of NiO diffraction intensity in NiO/ZrO$_2$ and NixZryO samples also indicates the interaction between nickel species and zirconium species in NixZryO samples.

To further figure out the effect of NiO incorporation on the morphology of NixZryO catalysts, SEM is employed in the characterization of NixZryO and NiO/ZrO$_2$ catalysts. As shown in the SEM images included in Fig. S1, the NixZryO catalysts with different Ni/Zr molar ratios show the similar surface morphology, which they are almost piled up by many tiny round particles. Among Ni1Zr3O, Ni1Zr1O and Ni3Zr1O, the particle size of Ni1Zr3O is minimum. However, these too small particles pile up into the solid Ni1Zr3O, which could lead the sharp decline of its surface area, pore volume and average pore diameter.

3.2. Catalytic performance of various catalysts

The activity and selectivity of various catalysts were tested for the hydrogenation of methyl levulinate (ML) to γ-valerolactone (GVL), and

Table 1
The Ni/Zr molar ratio and physico-chemical properties of NixZryO and NiO/ZrO$_2$ samples.

Entry	Sample	m$_{Ni}$ (%)	m$_{Zr}$ (%)	x/y	n$_{Ni}$/n$_{Zr}$[a]	SA[b] (m^2/g)	V$_{pore}$ (cm^3/g)	D$_{pore}$ (nm)
1	NiO	–	–	–	–	1.3	–	–
2	Ni10Zr1O	88	9.7	10	14.1	80.0	0.31	4.2
3	Ni5Zr1O	74	15	5	7.6	112.2	0.46	5.6
4	Ni3Zr1O	60	25	3	3.7	119.8	0.40	5.5
5	Ni2Zr1O	52	27	2	2.9	89.3	0.13	4.3
6	Ni1Zr1O	38	35	1	1.7	101.9	0.13	3.7
7	Ni1Zr2O	22	49	0.5	0.7	9.8	0.02	3.5
8	Ni1Zr3O	20	54	0.3	0.4	4.0	0.01	3.5
9	ZrO$_2$	–	–	–	–	66.7	0.12	4.0
10	NiO/ZrO$_2$	46	39	–	1.9	42.7	0.09	4.0
11	Used-catalyst	32	37	1	1.3	76.7	0.13	3.6

[a] The Ni/Zr molar ratio is calculated by ICP results.

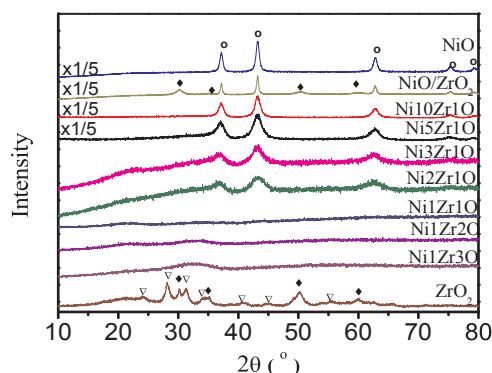[b] The BET surface area was determined by N$_2$ adsorption–desorption.

Fig. 1. XRD pattern for the NiO, ZrO$_2$, NiO/ZrO$_2$ and NixZryO catalysts. ○ NiO, ♦ c-ZrO$_2$, ▽ m-ZrO$_2$.

Table 2
Hydrogenation of methyl levulinate (ML) to γ-valerolactone (GVL) by different catalysts.

Entry	Catalyst	T (°C)	P (MPa)	C_{ML}(%)	Y_{GVL}(%)	S_{GVL}[a] (%)	Y_{LA}[a] (%)
1	NiO	150	0.3	64.2	60.9	95.3	–
2	Ni10Zr1O	150	0.3	79.5	76.1	95.7	–
3	Ni5Zr1O	150	0.3	86.4	82.2	95.1	–
4	Ni3Zr1O	150	0.3	99.1	95.0	96.0	–
5	Ni2Zr1O	150	0.3	96.9	92.1	95.1	–
6	Ni1Zr1O	150	0.3	96.2	95.2	99.0	–
7		110	0.3	38.1	23.7	62.2	–
8		130	0.3	66.3	55.1	83.1	–
9		170	0.3	98.7	96.9	98.2	–
10		200	0.3	> 99	98.2	98.2	
11		150	0.2	70.6	69.0	97.7	–
12		150	1.0	98.8	95.0	96.2	–
13		150	3.0	98.1	94.0	95.8	–
14	Ni2Zr3O	150	0.3	54.8	51.8	94.5	–
15	Ni1Zr2O	150	0.3	31.8	30.3	95.3	–
16	Ni1Zr3O	150	0.3	54.8	9.5	17.3	45.2
17	ZrO$_2$	150	0.3	81.6	3.6	4.4	78.0
18	NiO/ZrO$_2$	150	0.3	68.6	66.2	96.5	–
19	Raney Ni	150	0.3	89.7	86.2	96.1	–
20	Ni1Zr1O[b]	150	0.3	52.8	51.5	97.5	–
21	Ni-Mo/C[c]	200	10.0	94	80	84	
22	15% Ni/Al$_2$O$_3$[d]	200	5.0	100	92	92	–

Reaction condition: catalyst 0.05 g, ML 0.15 g, H$_2$O 5.0 g as solvent, 3 h.
[a] S_{GVL} is the selectivity to GVL. Y_{LA} is the yield of levulinic acid, which was produced by hydrolysis of methyl levulinate.
[b] The catalyst was reduced by hydrogen at 650 °C before used.
[c] See Ref. [44].
[d] See Ref. [29].

the results are given in Table 2. All catalysts were treated by hydrogen at 400 °C before used. When NiO was used as a catalyst, GVL yield was 53.7% (entry 1, Table 2). With the addition of zirconium to nickel species, the catalytic performance of NixZryO catalysts improved (entry 2, Table 2). It can be seen from Table 2, when decreasing the Ni/Zr molar ratio from 10 to 1, GVL yield enhanced from 76.1% (Ni10Zr1O) to 96.9% (Ni1Zr1O) (entries 2–6). However, if the Ni/Zr molar ratio was further reduced to 0.3, GVL yield lowered sharply to 9.5% on Ni1Zr3O catalyst (entry 15) while ML conversion still reached 54.8% with the main byproduct of levulinic acid (LA) due to the hydrolysis of ML. Therefore, zirconium species played a major role for the conversion of ML because GVL yield was 3.6% and LA yield was 78.0% (entry 17, Table 2) when ZrO$_2$ was used as a catalyst. Surprisingly, when NiO/ZrO$_2$ with a Ni/Zr molar ratio of 1 was used as a catalyst, the reaction proceeded with much lower GVL yield (entry 18, Table 2). It illustrates that there is some kind of interaction between nickel species and zirconium species in NixZryO samples unlike that of NiO/ZrO$_2$ sample. In addition, the yield of GVL is interestingly dropped to 51.5% when Ni1Zr1O catalyst was reduced at 650 °C (entry 20, Table 2).

The effects of reaction temperature and pressure on the activity of Ni1Zr1O are also presented in Table 2. As expected, the catalytic performance increased firstly with the temperature rise to up to 150 °C and then kept steady thereafter (entries 6–10, Table 2). A similar trend of Ni1Zr1O catalytic activity was found with the variation of the H$_2$ pressure. With the increase of H$_2$ pressure in water solvent, both ML conversion and GVL yield increased. The LA conversion rose to 98.7% and the highest GVL yield (96.9%) was obtained at 0.3 MPa. Further increasing H$_2$ pressure led to little change of Ni1Zr1O catalytic activity (entries 12 and 13, Table 2). Meanwhile, regarding the effect of H$_2$ pressure on the adsorption of ML molecule, we examined several additional adsorption models. From the obtained adsorption energies (Table S1), one can expect that H$_2$ pressure would causes a slight effect.

Considering the low BET surface area of NiO, commercial Raney Ni was used in the hydrogenation of ML to GVL (entry 19, Table 2). The yield of GVL was higher than that on NiO but still lower than that on Ni1Zr1O. Furthermore, it is also demonstrated that the NixZryO prepared in our work had better performance than other Ni-based catalysts reported in the literatures when the reaction was conducted under comparable severe reaction conditions (entries 21 and 22, Table 2).

3.3. The role of zirconium

The catalytic performance data of various NixZryO catalysts show that GVL yield over pure NiO catalyst was 53.7%, far less than that on NixZryO catalysts (x/y = 1 ~ 10). It indicates that the presence of zirconium will promote both ML conversion and GVL yield. In order to further study the role of zirconium in the NixZryO catalysts, the NixZryO catalysts were analyzed by various techniques including H$_2$-TPR, NH$_3$-TPD, XPS, and DFT.

3.3.1. H$_2$-TPR

The presence of metallic Ni is important for the catalytic hydrogenation of levulinate esters to GVL. In order to study the effect of zirconium on the reduction of nickel species in NixZryO, H$_2$-TPR analysis of various samples was carried out. The H$_2$-TPR profiles of various samples are shown in Figs. 2 and 3. As expected, no reduction signal could be seen on ZrO$_2$ sample (Fig. 2). For NiO sample, a reduction peak beginning at around 250 °C was detected associated with NiO reduction to metallic Ni. For NiO/ZrO$_2$ sample, the NiO reduction peak shifted to 270 °C. Compared with NiO, the slight shifting of NiO reduction peak is likely due to the weak interaction between nickel species and zirconium species. When zirconium was introduced to form NixZryO by the co-precipitation method, the reduction of nickel species changed greatly. As seen in Fig. 2, three peaks are found in the reduction of Ni1Zr1O sample. The reduction peak beginning at 270 °C is attributed to NiO reduction to Ni, similar to the NiO/ZrO$_2$ sample. A second peak of the H$_2$ consumption started at 390 °C and a third maximized at 480 °C, which may be resulted from the reduction of small nickel oxides generated due to the strong interaction between nickel species and zirconium species [29]. In the literatures, it is reported that the H$_2$-TPR pattern of the Ni/MgO catalyst shows three reduction peaks at a T$_{max}$ of
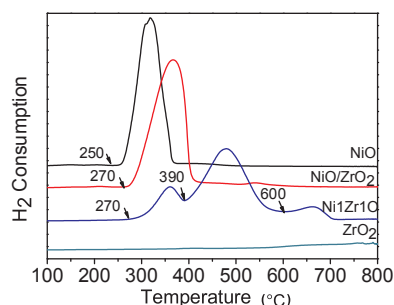

Fig. 2. H$_2$-TPR profiles of NiO, NiO/ZrO$_2$, Ni1Zr1O and ZrO$_2$ samples.
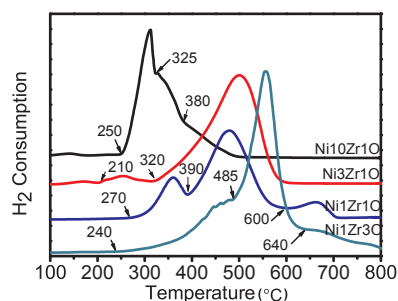
Fig. 3. H$_2$-TPR profiles of the NixZryO catalysts with different Ni/Zr ratio.

325, 600 and 775 °C due to the reduction of NiO located on the MgO surface, some Ni^{2+} ions with square-pyramidal coordination in the outermost layer of the catalyst structure, and the NiO–MgO (MgNiO$_2$) solid solution lattice, respectively [45]. So, the third H$_2$ consumption peak at high temperature (beginning at 600 °C) might be caused by the reduction of some Ni^{2+} ions with square-pyramidal coordination in the outermost layer of the catalyst structure or in the Ni$_m$Zr$_n$O quasi solid solution lattice.

The reduction behavior of the NixZryO catalysts with different Ni/Zr molar ratios was further investigated by H$_2$-TPR and showed in Fig. 3. For all NixZryO samples, the main H$_2$ consumption peak is shifted to high temperature compared to NiO and NiO/ZrO$_2$ catalysts. In the case of Ni10Zr1O sample, the H$_2$ consumption starts at 250 °C, increases continuously to 310 °C and ends at 500 °C. It is a broad peak including two shoulder peaks at 325 °C and 380 °C, respectively. With the increase of Zr content, three reduction peaks are detected over NixZryO samples except Ni3Zr1O (the latter two peaks maybe overlap), but all the reduction peaks shift to high temperatures. This maybe indicate that with the increase of the amount of zirconium, the interactions between nickel and zirconium species becomes stronger so that nickel species are more difficult to reduce. For Ni1Zr1O sample, nickel is easier to coordinate with zirconium or form Ni$_m$Zr$_n$O quasi solid solution than other NixZryO samples with less amount of zirconium. Three reduction peaks mean that there are different nickel species in Ni1Zr1O sample. Moreover, there is no obvious diffraction peak in XRD pattern of Ni1Zr1O, which also shows the strong synergism of nickel species and zirconium species.

3.3.2. NH$_3$-TPD

The temperature programmed desorption of ammonia (NH$_3$-TPD) profiles of ZrO$_2$ and NixZryO catalysts with different Ni/Zr molar ratios are shown in Fig. 4. The acid site distributions are mainly classified by temperature range as weak (< 250 °C), medium (250–400 °C) and strong (> 400 °C) acidic sites [46]. ZrO$_2$ catalyst shows one weak desorption peak at 300–400 °C indicating the presence of medium acidic sites. Both Ni10Zr1O and Ni1Zr1O catalyst show two desorption peaks located at 150–200 °C and 450–650 °C signifying the existence of medium and strong acidic sites. When the Ni/Zr molar ratio decreases to 0.3, the acid amount and strength increase greatly with a NH$_3$
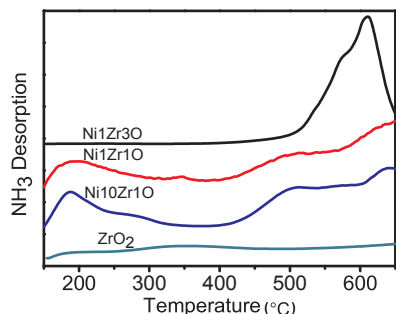

Fig. 4. NH$_3$-TPD profiles of ZrO$_2$, Ni10Zr1O, Ni1Zr1O and Ni1Zr3O catalysts.
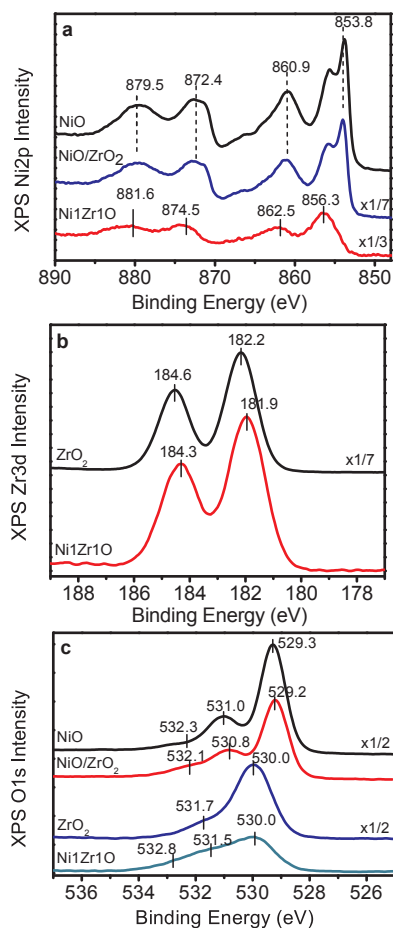

Fig. 5. XPS spectra of NiO, NiO/ZrO$_2$,Ni1Zr1O and ZrO$_2$ catalysts (a) Ni 2p, (b) Zr 3d and (c) O1s.

desorption peak centered at about 600 °C due to strong acidic sites. The acidity of catalytic systems plays a role in the hydrolysis of ML to produce levulinic acid (LA). When there are only acidic sites on the catalysts (ZrO$_2$), the hydrolysis of ML dominates the ML conversion reaction. It can be proved from Table 2, the main product is LA when using ZrO$_2$ or Ni1Zr3O as the catalyst, in which the yields of LA are 78.0% and 45.2%, respectively. If there are good hydrogenation sites with weak acidic sites (Ni1Zr1O) on the catalysts, the ML conversion reaction will lead to high GVL selectivity. In addition, the reaction pathway of ML into the byproduct LA on NiZrO was calculated. From the achieved free energies (Table S2) and free energy profile (Fig. S2), we can easily see that the LA formation is not favored relative to the GVL formation route, which accords well with the experimental conclusion that NiZrO possesses an extremely high selectivity.

3.3.3. XPS

The surface states of NiO, NiO/ZrO$_2$, Ni1Zr1O and ZrO$_2$ catalysts were analyzed by XPS. The spectra are shown in Fig. 5 and XPS elemental surface concentrations are listed in Table 3. Due to observe charging effects in XPS analysis, the binding energy scale was calibrated by adventitious carbon (284.8 eV).

In the Ni 2p region (Fig. 5 a), four characteristic features, i.e. Ni 2p$_{3/2}$ main peak and its satellite at 853.8 and 860.9 eV, respectively, as well as Ni 2p$_{1/2}$ main peak and its satellite at 872.4 and 879.5 eV, respectively, are observed on both NiO and NiO/ZrO$_2$ catalyst, which are in good accordance with the previous report [27]. The spectrum of NiO/ZrO$_2$ catalyst matches well with NiO, agreeing with the results of H$_2$-TPR in which both catalysts have the similar reduction profiles. For Ni1Zr1O, the detected Ni 2p$_{3/2}$ and Ni 2p$_{1/2}$ spectra shifted to high

Table 3

XPS elemental surface concentrations.

	Atomic concentrations[a] (at.%)			Atomic ratios	Binding Energy (eV)		
	Ni	Zr	O	Ni/Zr	O 1s[b]		
NiO	49.8	–	50.2	–	529.3	531.0 (0.36)	532.3 (0.15)
NiO/ZrO$_2$	46.9	1.0	52.1	48.4	529.2	530.8 (0.42)	532.1 (0.28)
Ni1Zr1O	13.9	15.7	70.4	0.9	530.0	531.5 (0.55)	532.8 (0.21)
ZrO$_2$	–	28.8	71.2	–	530.0	531.7 (0.21)	–

[a] Values of atomic concentrations are calculated after deducting the amount of adventitious carbon.

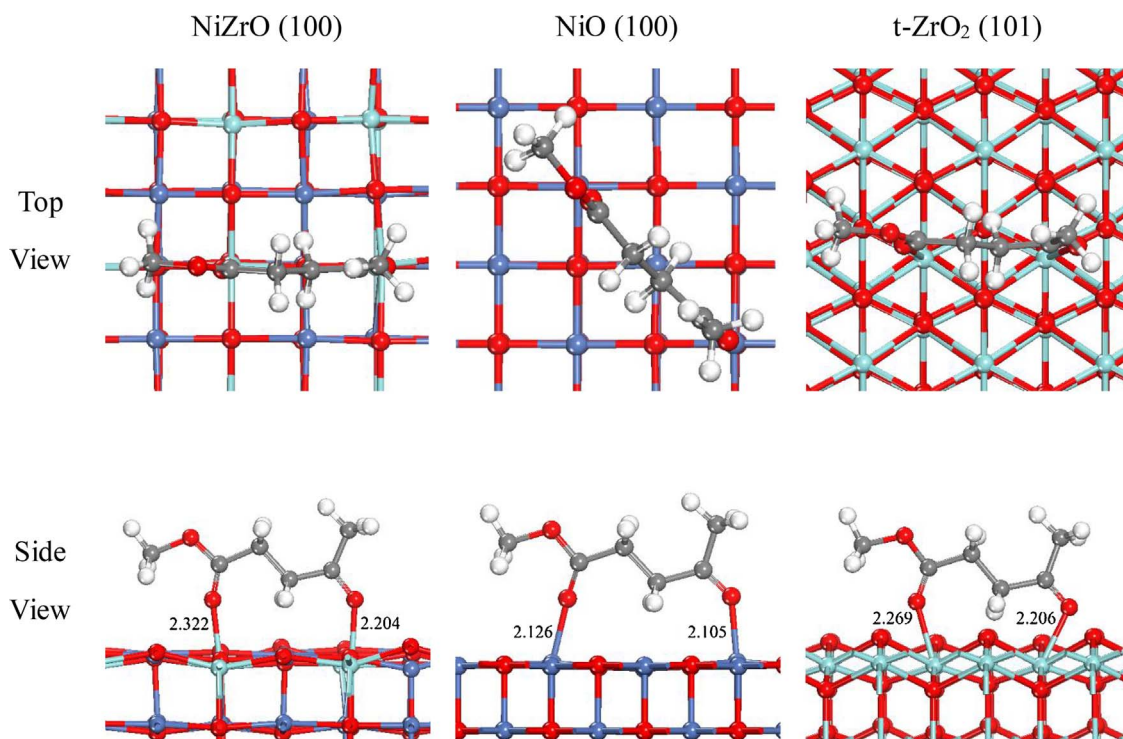[b] Numbers in parentheses are the peak area ratios of other O species to lattice oxygen (primary O 1s band).

Fig. 6. Top views and side views of the optimized structure of ML molecule on (a) NiZrO(100) plane, (b) NiO(100) and (c) t-ZrO$_2$(101) surface with the bidentate (O1-O2) configuration. The hydrogen, carbon, oxygen, zirconium and nickel atoms are represented in white, grey, red, light blue and dark blue, respectively. (For interpretation of the references to colour in this figure legend, the reader is referred to the web version of this article.)

binding energies, which are 856.3 eV and 874.5 eV (in reference NiO), respectively. In the previous report [47], three kinds of nickel species in Ca-promoted Ni/Al$_2$O$_3$ could be inferred from the following binding energies: NiAl$_2$O$_4$ (857.0 eV), NiO intimately interacting with support (856.0 eV) and bulk NiO (854.0 eV). Based on the above data, the existence of nickel ions with square-pyramidal coordination or in the Ni$_m$Zr$_n$O quasi solid solution lattice might be confirmed by XPS due to high Ni 2p$_{3/2}$ binding energy (856.3 eV), which is also fitting well with the results detected in H$_2$-TPR.

In the Zr 3d region (Fig. 5b), ZrO$_2$ catalyst shows two major peaks at binding energies of 182.2 and 184.6 eV corresponding to the core level Zr 3d$_{5/2}$ and Zr 3d$_{3/2}$ transitions, respectively. Similar patterns of Zr 3d$_{5/2}$ and Zr 3d$_{3/2}$ are detected on Ni1Zr1O surface. The trace of Zr 3d$_{5/2}$ and Zr 3d$_{3/2}$ curves at slightly lower binding energy (about 181.9 eV and 184.3 eV, respectively) in Ni1Zr1O than that in ZrO$_2$ might be the peaks of zirconium species interacted with nickel species. It is consistent with the variation reported by Schulz et al., in which the Zr 3d$_{5/2}$ and Zr 3d$_{3/2}$ ionization features decreased as cerium was doped into zirconium to form cerium zirconium solid solution [48].

In the O 1s region (Fig. 5c), after curve fitting procedures, O 1s peaks could be resolved into three features at around 529.2, 530.8 and 532.1 eV and results are summarized in Table 3. The primary O 1s

feature (529.2 eV) is characteristic of metal oxides, i.e. lattice oxygen [49]. It can be seen in Fig. 7 that the primary O 1s band (530.0 eV) of ZrO$_2$ is slightly higher than that of NiO (529.3 eV). For NiO/ZrO$_2$ and Ni1Zr1O samples, as shown in Table 3, nickel oxide is the dominated species on NiO/ZrO$_2$ surface while more zirconium species exists on Ni1Zr1O surface. Likewise, Fig. 8 shows that the primary O 1s band of NiO/ZrO$_2$ is similar to that of NiO, whereas Ni1Zr1O's primary O 1s band is almost identical to that of ZrO$_2$. The observed O 1s shoulder (> 532.0 eV) shifted to higher binding energy is the result of chemisorbed oxygen species [49] and this O 1s shift is highly variable and strongly dependent on the chemical compound [48]. Then the final band (532.1-532.8 eV) is suggested to arise from adsorbed surface −OH species or C−O species. Analysis of the remaining O 1s feature (530.8–531.7 eV) leads assignment to surface metal ion defect sites. It has been reported that the presence of Ce^{3+} surface defect sites on CeO$_2$ surface results in an additional O 1s band higher than the binding energy for lattice oxygen atoms [50]. The peak area ratio of O species with O 1s band at 530.8–531.7 eV to lattice oxygen (primary O 1s band) was calculated and shown in parentheses (in Table 3). The value on Ni1Zr1O (0.55) is higher than that on NiO (0.36) and NiO/ZrO$_2$ (0.42), indicating there are more metal ion surface defect sites on Ni1Zr1O.
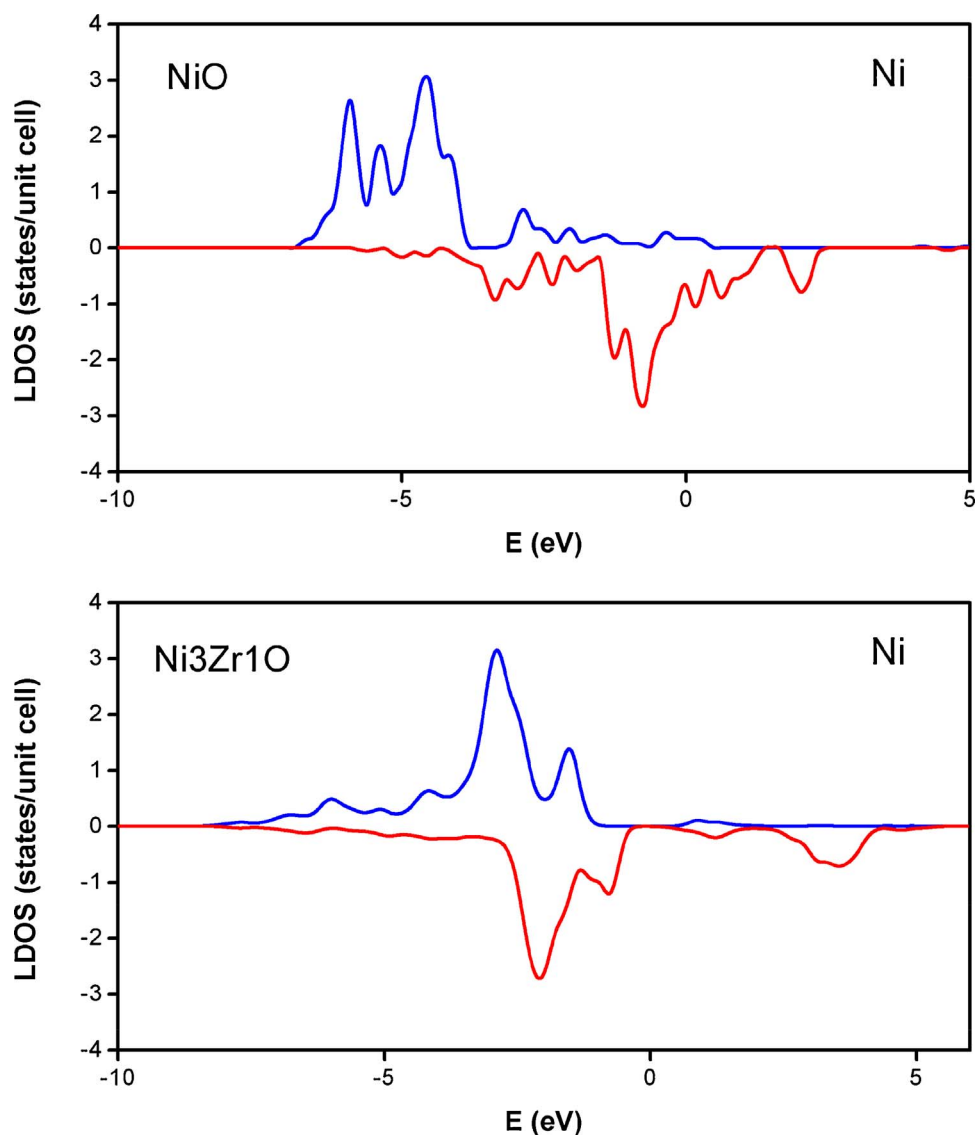
3.3.4. DFT calculation

It was noting that Heyden et al. computationally investigated the hydrogenation of LA to GVL and reported that the first hydrogenation step of LA toward an alkoxy intermediate (CH$_3$CH-(Ȯ)CH$_2$CH$_2$COOH), largely affected by LA adsorption, is the most rate controlling step over Ru(0001) surface [51]. Meanwhile, Li et al. found that Ni/NiO heterojunctions from the partial reduction of nickel oxide can efficiently catalyze LA hydrogenation to GVL and their theoretical calculations indicated that LA preferentially adsorbs on NiO surface, while H$_2$ preferentially adsorbs on the metallic Ni surface followed by the dissociation to atomic hydrogen [27]. Accordingly, the adsorption of ML molecule on NiO, NixZryO and ZrO$_2$ was studied by the first principles DFT calculations, respectively, aiming to evaluate and compare the catalytic abilities of these three catalysts. To describe NiO, the typically most stable (100) surface termination was used. For ZrO$_2$, there are three crystalline forms (c-ZrO$_2$, t-ZrO$_2$ and m-ZrO$_2$), and their most exposed surface configuration, *i.e.* the (111), (101) and (111), were selected, respectively. To model the NiZrO catalyst with a solid-solution structure, we adopted the doping strategy in which one of the four Ni atoms in the NiO bulk unit was substituted by Zr upon the subsequent lattice optimization, and (100) surface exposing both the Ni and Zr sites (Ni/Zr = 1) was cleaved and explored.

On these surfaces, the reactant ML could absorb at the metallic Lewis-acid site through its three terminal O in several possible configurations, such as the monodentate and bidentate ones. In the monodentate (or bidentate) adsorption configuration, each one (or either two) of the three terminal O atoms binds with the metallic sites correspondingly. As shown in Table 4, the adsorption energies of ML with all the different configurations on three catalyst surfaces were calculated. One can see that, on NiZrO(100), ML tends to follow the bidentate adsorption configuration and bind with two adjacent Zr atoms on NiZrO(100) using two acyl oxygens (O1–O2) (see Fig. 6, and Table S3), giving an adsorption energy as high as −1.82 eV, and the length of two formed Zr−O bonds are 2.204 Å and 2.322 Å, respectively. Importantly, it was demonstrated that NiZrO(100) exhibits the most powerful capacity of adsorbing and activating the reactant ML molecule in relative to the NiO(100) and three kinds of ZrO$_2$ surfaces (NiO: −0.97 eV; ZrO$_2$: −1.18 eV), verifying the experimentally observed improved activity of NiZrO catalyst.

To illustrate the origin of the enhanced ability of NiZrO(100), the local density of state (LDOS) of the surface Ni cation was calculated and compared with that on NiO(100). As shown in Fig. 7, it can be seen that the *d*-band of Ni on NiZrO(100) is more localized near the fermi level than that of NiO(100), implying that the higher energy levels of *d* orbital of NiZrO(100). Accordingly, one can anticipate that the *d* electrons would be more easily donated upon binding with the ML molecule, rationalizing the improved adsorption ability of NiZrO(100) surface compared with NiO(100).
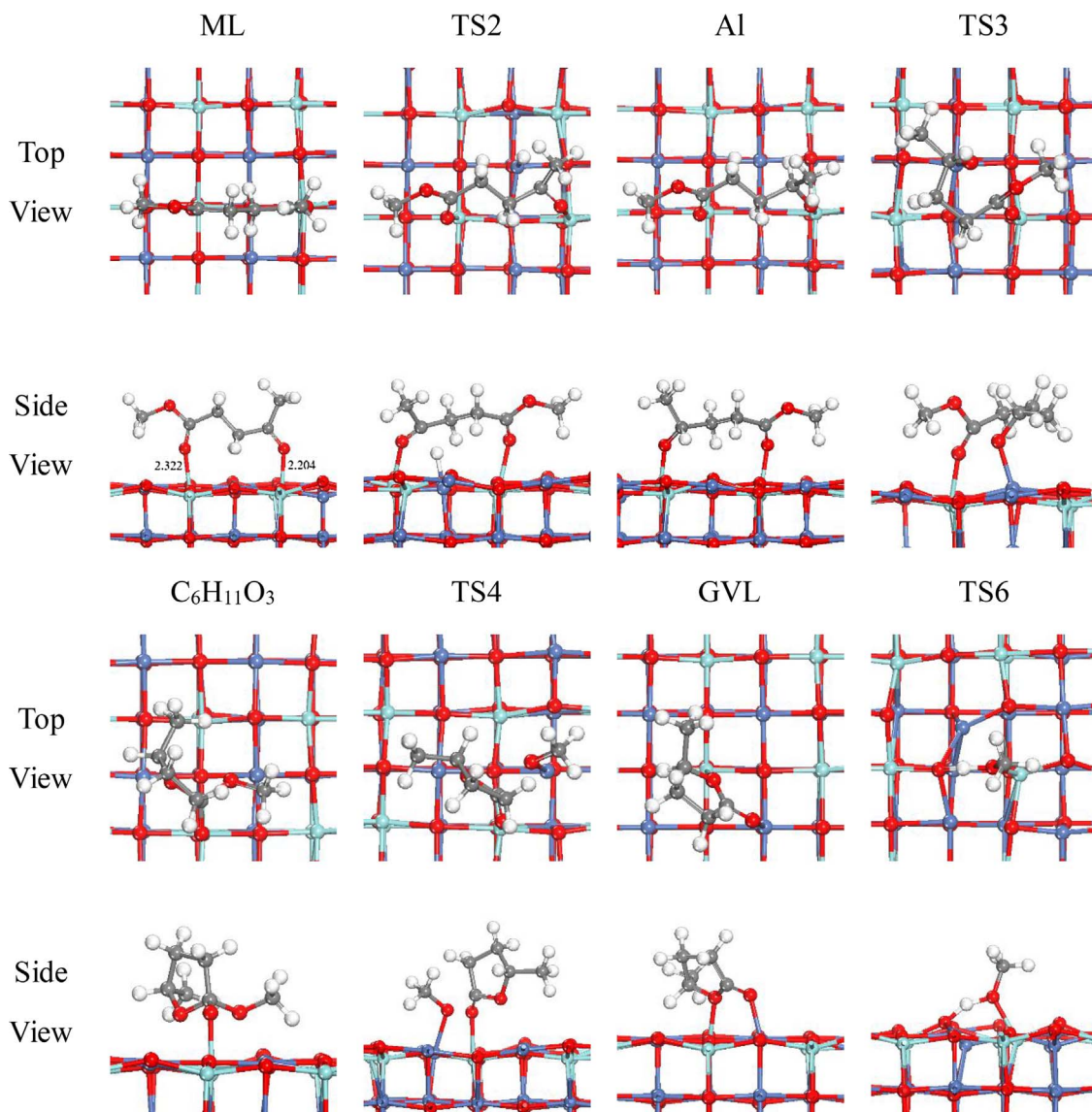
Fig. 8. The optimized geometries of key reaction intermediates and transition state structures involved in the conversion from ML to GVL on NiZrO(100), including the favored adsorption structure of the reactant ML and product GVL.

Table 4
The adsorption energies (in eV) of ML in different ways on NiO, ZrO$_2$ and NiZrO.

Cata.	monodentate			bidentate		
	O1[a]	O2[b]	O3[c]	O1-O2	O1-O3	O2-O3
NiO (100)	−0.51	−0.83	−0.78	−0.97	−0.93	−0.92
NiZrO (100)	−1.14	−1.39	−1.13	−1.82	−1.49	−1.21
c-ZrO$_2$ (111)	−0.60	−0.61	−0.49	−0.48	−0.52	−0.61
t-ZrO$_2$ (101)	−0.56	−0.71	−0.49	−0.93	−1.04	−0.85
m-ZrO$_2$ (111)	−0.92	−0.77	−0.77	−1.11	−1.02	−1.18

[a] O1 is acyl oxygen of methyl levulinate.
[b] O2 is double bond oxygen in ester bond of methyl levulinate.
[c] O3 is single bond oxygen in ester bond of methyl levulinate.

Table 5
Calculated free energy of reaction (ΔG) and activation barrier(E_a) at 423 K for the examined elementary steps of ML conversion into GVL on NiZrO and NiO catalyst surface.

step	reaction	NiZrO(100)		NiO(100)	
		ΔG (eV)	E_a (eV)	ΔG (eV)	E_a (eV)
R$_1$	$C_6H_{10}O_3$(g) + 2* → $C_6H_{10}O_3$** (ML adsorption)	0.41	/	1.18	/
R$_2$	$C_6H_{10}O_3$** + H* → $C_6H_{11}O_3$** + * (initial hydrogenation)	−1.78	0.31	0.05	0.47
R$_3$	$C_6H_{11}O_3$** → $C_6H_{11}O_3$* + * (cyclization)	0.81	1.27	−0.18	0.74
R$_4$	$C_6H_{11}O_3$* + 2* → $C_5H_8O_2$** + CH_3O* (breaking C−OCH$_3$ bond)	−0.34	0.57	0.15	0.32
R$_5$	$C_5H_8O_2$** → $C_5H_8O_2$(g) + 2* (GVL desorption)	−0.65	/	−1.06	/
R$_6$	CH_3O* + H* → CH_3OH* + * (CH_3O hydrogenation)	0.12	0.28	−0.50	0.43
R$_7$	CH_3OH* → CH_3OH(g) + * (methanol desorption)	0.56	/	−0.45	/

To provide a more comprehensive understanding of ML conversion on NiZrO catalyst, the overall reaction pathways of ML conversion into γ-valerolactone (GVL) on NiZrO(100) and pure NiO(100) catalyst were computationally examined and compared. The detailed elementary steps were shown in Table 5, which mainly contains (i) ML adsorption and hydrogenation, forming an alkoxy intermediate (Al), (ii) the ring
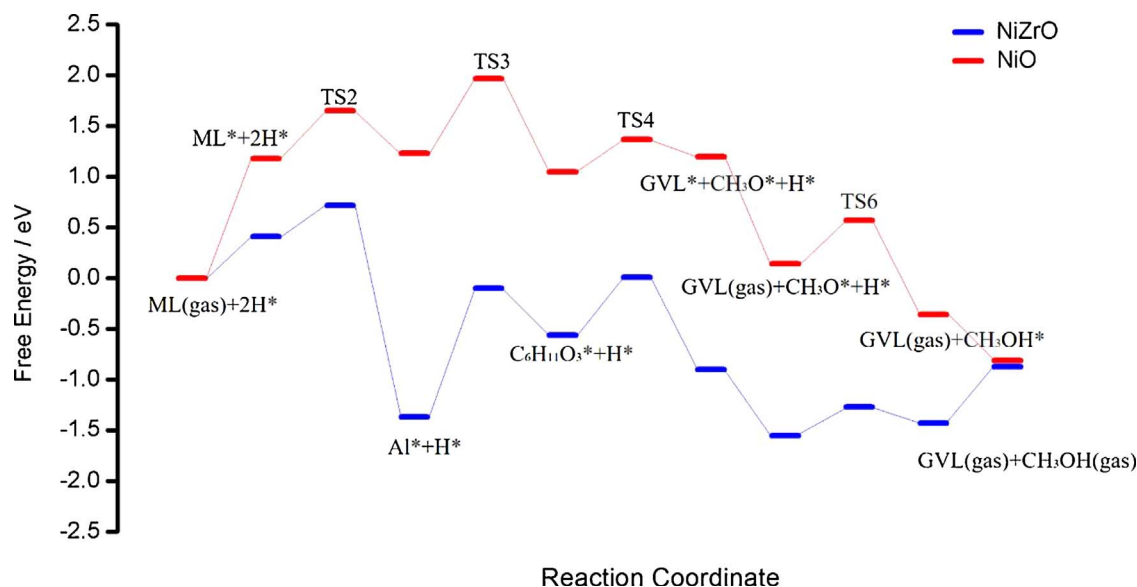
Fig. 9. The Gibbs free energy profiles of ML conversion into GVL on NiZrO(100) (blue line) and pure NiO(100) (red line), following the reaction pathways listed in Table 5. The temperature was taken as 423 K as used in the experiments. (For interpretation of the references to colour in this figure legend, the reader is referred to the web version of this article.)
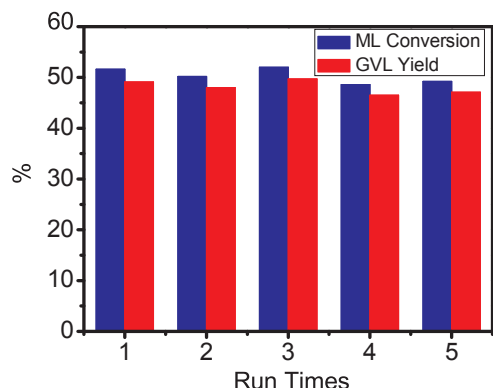

Fig. 10. Recyclability of Ni1Zr1O catalyst for the hydrogenation of ML to GVL. (Reaction conditions: 0.15 g ML, 0.05 g catalyst Ni1Zr1O, 5.0 g H_2O, 0.3 MPa H_2, 150 °C, 1 h).

closure reaction of A1 to generate $C_6H_{11}O_3$ ($C_4OH_5(CH_3)(O\cdot)(CH_3)$) and (iii) the cleavage of the C−OCH_3 bond at the C_1 site of the intermediate $C_6H_{11}O_3$, leading to the ultimate product GVL. The optimized structures of the key intermediates and transition states (TS) were illustrated in Fig. 8.

From the obtained free energy profile (Fig. 9), one can see some information as follows. (i) On NiZrO catalyst, the conversion of ML into GVL is a relatively easy process, which corresponds to an overall downhill profile without evidently high barrier, according with the good catalytic activity of NiZrO catalyst in the experiment; (ii) the whole free energy profile of NiZrO catalyst is below that on the pure NiO catalyst, illustrating the improved catalyst activity of NiZrO compared with NiO; (iii) the rate-determining step was located to the adsorption of ML molecule (R1) and its initial hydrogenation of acyl group (R2) on either NiZrO or NiO catalyst, which correspond to the highest energy point in the whole free energy profile, and it further rationalizes that the adsorption energy of the reactant ML molecule can serve as an activity descriptor.

3.4. Catalytic stability

The recyclability of Ni1Zr1O catalyst was evaluated by repeating the ML hydrogenation to GVL with the same catalyst. After each reaction cycle, the upper liquid phase was collected and analyzed by GC.

The catalyst was washed by ethanol and water for the next run. Here, in order to observe the change of catalytic performance for Ni1Zr1O more clearly and quickly, 1 h, which gives the ML conversion of ~50%, was chosen as the reaction time to test the catalytic stability in the hydrogenation of ML to GVL. The GVL yield and the ML conversion obtained from each cycle are shown in Fig. 10. There was no significant change in the GVL yield and ML conversion. Only a slight drop after five successive runs was observed. The results show the feasibility of Ni1Zr1O catalyst for the ML hydrogenation to GVL.

The Ni/Zr molar ratio and physico-chemical properties of the used Ni1Zr1O catalyst after 5 cycle reactions have been examined and the data are given in Table 1. It can be seen that the BET surface area, pore volume and average pore diameter fall slightly. But the Ni/Zr molar ratio goes down obviously from 1.7 to 1.3. This indicates that there is a loss of nickel component during the repeated reactions.

In addition, XRD, SEM, TEM and TG-DTA of the used Ni1Zr1O have been characterized. As shown in Fig. S3, the diffraction lines at $2\theta = 44.5$ and 76.4° due to metallic Ni phase is observed for the reduced Ni1Zr1O sample before hydrogenation of ML. By comparison, the intensity of ZrO_2 diffraction lines of the used Ni1Zr1O also became strong.

SEM and TEM are used to characterize the morphology of the used Ni1Zr1O catalyst (Fig. S4 and Fig. S5b). The results showed that the surface structure of the used Ni1Zr1O catalyst is still unchanged compared with the fresh Ni1Zr1O sample (see Fig. S1 b and b1, Fig. S5a). This is consistent with the previous physico-chemical results.

To quantify the coke deposited during 5 cycle reactions, TG-DTA of spent Ni1Zr1O catalyst is performed and reported in Fig. S6. These results reveal a small amount of carbon accumulation on spent Ni1Zr1O surface after 5 cycle reactions.

Overall, the little drop of catalytic performance for the spent Ni1Zr1O is mainly due to the leaching of nickel component. Therefore, how to prevent the loss of nickel component in NixZryO catalysts is a difficult but important problem.

4. Conclusion

Several NixZryO catalysts were prepared by a co-precipitation method and tested in the hydrogenation of methyl levulinate (ML) to prepare γ-valerolactone (GVL). The performance of the prepared catalysts was found to depend on their Ni/Zr molar ratio. After

optimization, it was found that the hydrogenation reaction was best carried out with Ni1Zr1O (Ni/Zr = 1:1) in water at 150 °C and 0.3 MPa H_2, which gave a GVL yield of 96.9%. The introduction of zirconium to nickel oxide remarkably enhanced the catalyst's performance and eliminated the need to used high pressure (> 3 MPa) in the hydrogenation reaction.

The role of zirconium in NixZryO was further investigated by comparison of the catalyst with Raney Ni, NiO, ZrO_2, and NiO/ZrO_2 (prepared by wet impregnation). The XRD, H_2-TPR and XPS analyses showed that three kinds of nickel species existed in Ni1Zr1O: NiO, small nickel oxides intimately interacting with zirconium species, and nickel species with square-pyramidal coordination or in the Ni_mZr_nO quasi solid solution lattice. Subsequent DFT calculations showed that the formed Ni_mZr_nO quasi solid solution was more suitable for the adsorption of ML than pure nickel and zirconium oxides. In particular, the yield of GVL dropped when the Ni_mZr_nO quasi solid solution in the catalyst was destroyed by raising pre-reduction temperature from 400 °C to 650 °C, which proved that the formed Ni_mZr_nO quasi solid solution assisted in ML adsorption and activation. It could be inferred that when a certain amount of zirconium was introduced (e.g., Ni/Zr = 1), part of the nickel coordinated with zirconium or formed Ni_mZr_nO quasi solid solution. In the catalytic hydrogenation of ML to prepare GVL, the synergy between metallic nickel, which activated H_2, and the Ni − O − Zr species, which activated ML, improved the performance of the catalyst notably. Furthermore, the Ni_1Zr_1O catalyst showed good catalytic stability, as it retained good activity after five cycles of hydrogenation reaction of ML.

Acknowledgements

Appendix A. Supplementary data

Supplementary data associated with this article can be found, in the online version, at https://doi.org/10.1016/j.apcatb.2018.01.010.

References

[1] D.M. Alonso, S.G. Wettstein, J.A. Dumesic, Gamma-valerolactone, a sustainable platform molecule derived from lignocellulosic biomass, Green Chem. 15 (2013) 584–595.
[2] K. Yan, Y.Y. Yang, J.J. Chai, Y. Lu, Catalytic reactions of gamma-valerolactone: a platform to fuels and value-added chemicals, Appl. Catal. B: Environ. 179 (2015) 292–304.
[3] M.J. Climent, A. Corma, S. Iborra, Conversion of biomass platform molecules into fuel additives and liquid hydrocarbon fuels, Green Chem. 16 (2014) 516–547.
[4] J.Q. Bond, A.A. Upadhye, H. Olcay, G.A. Tompsett, J. Jae, R. Xing, D.M. Alonso, D. Wang, T. Zhang, R. Kumar, A. Foster, S.M. Sen, C.T. Maravelias, R. Malina, S.R.H. Barrett, R. Lobo, C.E. Wyman, J.A. Dumesic, G.W. Huber, Production of renewable jet fuel range alkanes and commodity chemicals from integrated catalytic processing of biomass, Energy Environ. Sci. 7 (2014) 1500–1523.
[5] H. Mehdi, V. Fabos, R. Tuba, Integration of homogeneous and heterogeneous catalytic processes for a multi-step conversion of biomass: from sucrose to levulinic acid gamma-valerolactone, 1,4-pentanediol, 2-methyl-tetrahydrofuran, and alkanes, Top. Catal. 48 (2008) 49–54.
[6] L. Deng, J. Li, D.M. Lai, Catalytic conversion of biomass-Derived carbohydrates into gamma-Valerolactone without using an external H_2 supply, Angew. Chem. Int. Ed. 48 (2009) 6529–6532.
[7] B. Hernández, J. Iglesias, G. Morales, M. Paniagua, C. López-Aguado, J.L. García Fierro, P. Wolf, I. Hermans, J.A. Melero, One-pot cascade transformation of xylose into γ-valerolactone (GVL) over bifunctional Bránsted-Lewis Zr-Al-beta zeolite, Green Chem. 18 (2016) 5777–5781.
[8] H. Li, Z. Fang, S. Yang, Direct catalytic transformation of biomass derivatives into biofuel component gamma-valerolactone with magnetic nickel-zirconium nanoparticles, ChemPlusChem 81 (2016) 135–142.
[9] D.J. Braden, C.A. Henao, J. Heltzel, C.T. Maravelias, J.A. Dumesic, Production of liquid hydrocarbon fuels by catalytic conversion of biomass-derived levulinic acid, Green Chem. 13 (2011) 1755–1765.
[10] E.I. Guerbuez, D.M. Alonso, J.Q. Bond, J.A. Dumesic, Reactive extraction of levulinate esters and conversion to gamma-valerolactone for production of liquid fuels, ChemSusChem 4 (2011) 357–361.
[11] H. Li, Z. Fang, J. Luo, Direct conversion of biomass components to the biofuel methyl levulinate catalyzed by acid-base bifunctional zirconia-zeolites, Appl. Catal. B: Environ. 200 (2017) 182–191.
[12] Z.P. Yan, L. Lin, S.J. Liu, Synthesis of gamma-valerolactone by hydrogenation of biomass-derived levulinic acid over Ru/C catalyst, Energy Fuels. 23 (2009) 3853–3858.
[13] A.M.R. Galletti, C. Antonetti, De Luise, Valentina, A sustainable process for the production of gamma-valerolactone by hydrogenation of biomass-derived levulinic acid, Green Chem. 14 (2012) 688–694.
[14] P.P. Upare, J.M. Lee, H. Wang, W. Dong, Selective hydrogenation of levulinic acid to gamma-valerolactone over carbon-supported noble metal catalysts, J. Ind. Eng. Chem. 17 (2011) 287–292.
[15] S.G. Wettstein, J.Q. Bond, D.M. Alonso, H.N. Pham, A.K. Datye, J.A. Dumesic, RuSn bimetallic catalysts for selective hydrogenation of levulinic acid to gamma-valerolactone, Appl. Catal. B: Environ. 117 (2012) 321–329.
[16] M. Sudhakar, V.V. Kumar, G. Naresh, M.L. Kantam, S.K. Bhargava, A. Venugopal, Vapor phase hydrogenation of aqueous levulinic acid over hydroxyapatite supported metal (M = Pd, Pt Ru, Cu, Ni) catalysts, Appl. Catal. B: Environ. 180 (2016) 113–120.
[17] R.A. Bourne, J.G. Stevens, J. Ke, Maximising opportunities in supercritical chemistry: the continuous conversion of levulinic acid to gamma-valerolactone in CO_2, Chem. Commun. 44 (2007) 4632–4634.
[18] L. Deng, Y. Zhao, J. Li, Conversion of levulinic acid and formic acid into gamma-valerolactone over heterogeneous catalysts, ChemSusChem 3 (2010) 1172–1175.
[19] M. Chia, J.A. Dumesic, Liquid-phase catalytic transfer hydrogenation and cyclization of levulinic acid and its esters to gamma-valerolactone over metal oxide catalysts, Chem. Commun. 47 (2011) 12233–12235.
[20] X. Tang, H.W. Chen, L. Hu, W.W. Hao, Y. Sun, X.H. Zeng, L. Lin, S.J. Liu, Conversion of biomass to gamma-valerolactone by catalytic transfer hydrogenation of ethyl levulinate over metal hydroxides, Appl. Catal. B: Environ. 147 (2014) 827–834.
[21] F.K. Li, L.J. France, Z.P. Cai, Y.W. Li, S.J. Liu, H.M. Lou, J.X. Long, X.H. Li, Catalytic transfer hydrogenation of butyl levulinate to gamma-valerolactone over zirconium phosphates with adjustable Lewis and Bronsted acid sites, Appl. Catal. B: Environ. 214 (2017) 67–77.
[22] X. Tang, Z. Li, X.H. Zeng, Y.T. Jiang, S.J. Liu, T.Z. Lei, Y. Sun, L. Lin, InSitu catalytic hydrogenation of biomass-derived methyl levulinate to −valerolactone in methanol, ChemSusChem 8 (2015) 1601–1607.
[23] A.M. Hengne, V.R. Chandrashekhar, Cu-ZrO₂ nanocomposite catalyst for selective hydrogenation of levulinic acid and its ester to γ-valerolactone, Green Chem. 14 (2012) 1064–1072.
[24] S. Ishikawa, D.R. Jones, S. Iqbal, C. Reece, D.J. Morgan, D.J. Willock, P.J. Miedziak, J.K. Bartley, J.K. Edwards, T. Murayama, W. Ueda, G.J. Hutchings, Identification of the catalytically active component of Cu-Zr-O catalyst for the hydrogenation of levulinic acid to gamma-valerolactone, Green Chem. 19 (2017) 225–236.
[25] Q. Xu, X.L. Li, T. Pan, C.G. Yu, J. Deng, Q.X. Guo, Y. Fu, Supported copper catalysts for highly efficient hydrogenation of biomass-derived levulinic acid and gamma-valerolactone, Green Chem. 18 (2016) 1287–1294.
[26] B. Zhang, Y. Chen, J.W. Li, E. Pippel, H.M. Yang, Z. Gao, Y. Qin, High efficiency Cu-ZnO hydrogenation catalyst: the tailoring of Cu-ZnO interface sites by molecular layer deposition, ACS Catal. 5 (2015) 5567–5573.
[27] S. Song, S.K. Yao, J.H. Cao, L. Di, G.J. Wu, N.J. Guan, L.D. Li, Heterostructured Ni/NiO composite as a robust catalyst for the hydrogenation of levulinic acid to gamma-valerolactone, Appl. Catal. B: Environ. 217 (2017) 115–124.
[28] K. Hengst, D.A.J.M. Ligthart, D.E. Doronkin, K.M. Walter, W. Kleist, E.J.M. Hensen, J.D. Grunwaldt, Continuous synthesis of gamma-valerolactone in a trickle-bed reactor over supported nickel catalysts, Ind. Eng. Chem. Res. 56 (2017) 2680–2689.
[29] K. Hengst, M. Schubert, H.W.P. Carvalho, C.B. Lu, W. Kleist, J.D. Grunwaldt, Synthesis of gamma-valerolactone by hydrogenation of levulinic acid over supported nickel catalysts, Appl. Catal. A: Gen. 502 (2015) 18–26.
[30] K. Shimizu, S. Kannoa, K. Kona, Hydrogenation of levulinic acid to γ-valerolactone by Ni and MoOx co-loaded carbon catalysts, Green Chem. 16 (2014) 3899–3903.
[31] G.N. Yun, A. Takagaki, R. Kikuchi, S.T. Oyama, Hydrodeoxygenation of gamma-valerolactone on transition metal phosphide catalysts, Catal. Sci. Technol. 7 (2017) 281–292.
[32] C. Li, G.Y. Xu, Y.X. Zhai, X.H. Liu, Y.F. Ma, Y. Zhang, Hydrogenation of biomass-derived ethyl levulinate into gamma-valerolactone by activated carbon supported bimetallic Ni and Fe catalysts, Fuel 203 (2017) 23–31.
[33] G. Chieffi, M. Braun, D. Esposito, Continuous reductive amination of biomass-derived molecules over carbonized filter paper-supported FeNi alloy, ChemSusChem 8 (2015) 3590–3594.
[34] Rodiansono, M.D. Astuti, T. Hara, N. Ichikuni, S. Shimazu, Efficient hydrogenation of levulinic acid in water using a supported Ni-Sn alloy on aluminium hydroxide catalysts, Catal. Sci. Technol. 6 (2016) 2955–2961.
[35] L.C. Liu, F. Gao, P. Concepcion, A. Corma, A new strategy to transform mono and bimetallic non-noble metal nanoparticles into highly active and chemoselective hydrogenation catalysts, J. Catal. 350 (2017) 218–225.
[36] J. Quiroz, E.F. Mai, V.T. da Silva, Synthesis of nanostructured molybdenum carbide as catalyst for the hydrogenation of levulinic acid to gamma-valerolactone, Top. Catal. 59 (2016) 2–4.

[37] G. Kresse, J. Furthmüller, Efficiency of ab-initio total energy calculations for metals and semiconductors using a plane-wave basis set, J. Comput. Mater. Sci. 6 (1996) 15–50.

[38] J.P. Perdew, K. Burke, M. Ernzerhof, Generalized gradient approximation made simple, Phys. Rev. Lett. 77 (1996) 3865–3868.

[39] P.E. Blöchl, Projector augmented-wave method, Phys. Rev. B 50 (1994) 17953–17979.

[40] A.M. Ferrari, C. Pisani, F. Cinquini, Cationic and anionic vacancies on the NiO (100) surface: DFT + U and hybrid functional density functional theory calculations, J. Chem. Phys. 127 (17) (2007) 174711.

[41] S. Grimme, Semiempirical GGA-type density functional constructed with a long-range dispersion correction, J. Comput. Chem. 27 (2006) 1787–1799.

[42] A. Alavi, P. Hu, T. Deutsch, P.L. Silvestrelli, J. Hutter, CO oxidation on Pt(111): an ab initio density functional theory study, Phys. Rev. Lett. 80 (1998) 3650–3653.

[43] W. Ciptonugroho, M.G. Al-Shaal, J.B. Mensah, R. Palkovits, One pot synthesis of WOx/mesoporous-ZrO$_2$ catalysts for the production of levulinic-acid esters, J. Catal. 340 (2016) 17–29.

[44] B.P. Pinto, A.L.L. Fortuna, C.P. Cardoso, C.J.A. Mota, Hydrogenation of levulinic acid (LA) to γ-valerolactone (GVL) over Ni-Mo/C catalysts and water-soluble

[45] T. Furusawa, A. Tsutsumi, Appl. Catal. A. Gen. 278 (2005) 207–212.

[46] A. Boreave, A. Auroux, C. Guimon, Nature and strength of acid sites in HY zeolites: a multitechnical approach, Microporous Mater. 11 (1997) 275–291.

[47] Z. Hou, O. Yokota, T. Tanaka, T. Yashima, Characterization of Ca-promoted Ni/-Al$_2$O$_3$ catalyst for CH$_4$ reforming with CO$_2$, Appl. Catal. A: Gen. 253 (2003) 381–387.

[48] A.E. Nelsona, K.H. Schulz, Comparison of Co/MgO and Ni/MgO catalysts for the steam reforming of naphthalene as a model compound of tar derived from biomass gasification, Appl. Surf. Sci. 210 (2003) 206–221.

[49] A. Platau, L.I. Johansson, A.L. Hagstrom, S.E. Karlsson, S.B.M. Hagstrom, Oxidation of cerium and titanium studied by photoelectron spectroscopy, Surf. Sci. 63 (1977) 153–161.

[50] A. Pfau, K.D. Schierbaum, The electronic structure of stoichiometric and reduced CeO$_2$ surfaces: an XPS, UPS and HREELS study, Surf. Sci. 321 (1994) 71–80.

[51] O. Mamun, E. Walker, M. Faheem, J.Q. Bond, A. Heyden, Theoretical investigation of the hydrodeoxygenation of levulinic acid to gamma-valerolactone over Ru (0001), ACS Catal. 1 (2017) 215–228.

solvent systems, Catal. Lett. 147 (2017) 751–757.